Nanoscale

PAPER

View Article Online
View Journal | View Issue

Cite this: *Nanoscale*, 2021, **13**, 15699

Rapid bacterial elimination achieved by sonodynamic Au@Cu_2O hybrid nanocubes†

Yizhou Zhu,‡[a] Wanglong Hong,‡[b] Xiangmei Liu,*[b] Lei Tan,[b] Jun Wu,[c] Congyang Mao,[a] Yiming Xiang,[a] Shuilin Wu,*[d] Kenneth M. C. Cheung[a,c] and Kelvin W. K. Yeung *[a,c]

Although efforts have been devoted to develop new antibacterial agents and techniques, the challenge of bacterial infection remains unresolved and is even increasing. Sonodynamic therapy (SDT) driven by ultrasound (US) has demonstrated effectiveness in terms of penetration and it can help to clinically address the problem of deep tissue bacterial infection. In recent years, a variety of sonosensitizers, which were originally designed for photodynamic therapy, have been adopted for SDT. Yet, their unstable chemical stability and ineffective electron–hole separation are not favorable for clinical applications. Hence, we designed a new type of antibacterial sonosensitizer—namely, Au@Cu_2O hybrid nanocubes—in which an interfacial Schottky junction was built between a p-type semiconductor Cu_2O and a noble metal Au. When US stimulation was applied, the electrons from Cu_2O could be excited at the junction and transferred to Au. Since the formed Schottky barrier could block the backflow of US-excited electrons, a prolonged electron–hole separation can be successfully established. Additionally, because of the boosted sonocatalytic activity, the Au@Cu_2O hybrid nanocubes could produce a large amount of reactive oxygen species (ROS), which are subject to US stimulation. Furthermore, we found that the sonocatalytic activity of the Au@Cu_2O hybrid nanocubes could be reinforced by increasing the amount of Au, enabling 99.67% of *Staphylococcus aureus* (*S. aureus*) to be killed by US stimulation for 15 minutes. The cytocompatibility of Au@Cu_2O hybrid nanocubes was improved by a red blood cell membrane (RBC) coating over the surface, and the membrane did not sacrifice its superior antibacterial properties.

Received 12th July 2021,
Accepted 24th August 2021

DOI: 10.1039/d1nr04512a

rsc.li/nanoscale

1. Introduction

Bacterial infections have become a major threat to public health.[1,2] Conventionally, a variety of antibiotic treatments have been applied to combat different types of bacteria. However, the abuse of antibiotics has resulted in the development of drug-resistant bacteria. Thus, there is a growing demand to identify new antibacterial agents or innovative techniques for disinfection. Inorganic metal nanoparticles,[3,4] metal oxide,[5,6] and organic antibacterial agents[7] can exhibit a broad spectrum of antibacterial activities. However, these non-antibiotic agents are ineffective within a short period of exposure time, and they may be toxic to human tissues when applied clinically.[8]

In recent years, the exogenous antibacterial approach has become a promising antibiotic-free antibacterial strategy with high maneuverability and an ability to rapidly eliminate bacteria.[9] Photodynamic treatment (PDT), one example of this approach, is based on materials that can generate reactive oxygen species (ROS) under light stimulation to eliminate bacteria.[10,11] This therapy can elevate the oxidative stress within bacteria and then cause bacteria protein and DNA/RNA damage, thereby rapidly killing bacteria. This approach may reduce the risk of antibiotic-resistant bacteria.[12–15] However, when bacterial infection occurs in deep tissues, the antibacter-

[a]*Department of Orthopaedics & Traumatology, Li Ka Shing Faculty of Medicine, The University of Hong Kong, Pokfulam, Hong Kong, 999077, China. E-mail: wkkyeung@hku.hk*
[b]*Biomedical Materials Engineering Research Center, Collaborative Innovation Center for Advanced Organic Chemical Materials Co-constructed by the Province and Ministry, Hubei Key Laboratory of Polymer Materials, Ministry of Education Key Laboratory for the Green Preparation and Application of Functional Materials, School of Materials Science & Engineering, Hubei University, Wuhan, 430062, China. E-mail: xm.liu@hubu.edu.cn*
[c]*Shenzhen Key Laboratory for Innovative Technology in Orthopaedic Trauma, Department of Orthopaedics and Traumatology, The University of Hong Kong-Shenzhen Hospital, Shenzhen, 518053, China*
[d]*School of Materials Science & Engineering, the Key Laboratory of Advanced Ceramics and Machining Technology by the Ministry of Education of China, Tianjin University, Tianjin, 300072, China. E-mail: shuilinwu@tju.edu.cn*
†Electronic supplementary information (ESI) available. See DOI: 10.1039/d1nr04512a
‡These authors contribute equally to this paper.

ial qualities induced by PDT become limited due to the penetration power of light sources.[16,17]

Sonodynamic therapy (SDT) driven by ultrasound (US) may be able to compensate for the limitations of PDT. The therapeutic US can penetrate into deep tissues, as its tissue attenuation coefficient is low. Hence, the signal can pass through tissues without energy loss or tissue damage.[18,19] As a result, recently, SDT has been considered as a strategy for eliminating bacterial biofilm.[20,21] The bacterial killing mechanism of SDT is similar to PDT in that it entirely depends on ROS generation. Sonosensitizers, such as titanium dioxide and bismuth oxybromide nanoparticles, can be activated by acoustic waves, and its mechanism relies on the jump of exciting electrons from their valence band (VB) to the conduction band (CB).[21,22] This causes the separation of electrons and holes, which leads to a reaction with water and oxygen for ROS generation.[23] However, it is well known that the rapid recombination of electrons and holes impedes the generation of ROS. Fortunately, this challenge can be resolved by improving the separation efficiency of US-induced electron–hole pairs.

Previous studies have discovered that coupling noble metals (*e.g.*, Ag, Au, and Pt) onto a semiconductor surface could improve electron–hole separation efficiency, thereby enhancing photocatalytic performance. The working mechanism allows those noble metals to trap the photoexcited electrons from the CB of the semiconductor and then prevent the recombination of electron–hole pairs.[24,25] For example, Cu_2O is a widely used p-type semiconductor with a bandgap of 2.17 eV, which has been used as a photocatalyst for water splitting and organic contamination degradation.[26,27] To improve the low electron migration rate and photocatalytic activity of Cu_2O, previous studies had considered to couple Au as an enhancer[28,29] and the modified Cu_2O nanoparticles had been applied in various areas such as environmental purification, solar energy conversion and gas sensing.[30–33] Hence, we believe that the ROS generation induced by sonosensitizers can be also enhanced by incorporating noble metals onto the surface of a semiconductor material due to the enhanced electron–hole separation efficiency.

Herein, we designed a series of Au@Cu_2O hybrid nanocubes in which Au nanoparticles were incorporated onto the surface of Cu_2O. After synthesis, a Schottky contact was found at the interface of the metal cocatalysts (Au) and its counterpart semiconductor (Cu_2O). We determined that the electron structure and sonodynamic properties could be manipulated by changing the ratio of Au on the Cu_2O nanocube surface. The different electron states, sonodynamic properties, ROS generation efficiency, and antibacterial ability of various Au@Cu_2O nanocubes were also investigated. To improve biocompatibility, we coated the surface of Au(25)@Cu_2O nanomaterials with a layer of red blood cell (RBC) membranes. We believe that a metal semiconductor with a Schottky junction designed for SDT is a promising approach to eliminate the bacterial infection, particularly for patients with deep wound infections.

2. Materials and methods

2.1. Reagents

Copper (II) chloride dihydrate ($CuCl_2$), sodium hydroxide (NaOH), ascorbic acid, sodium sulfate (Na_2SO_4), and tetrachloroauric (III) acid hydrate ($HAuCl_4$) were purchased from Sinopharm Chemical Reagent Co., Ltd (Shanghai, China). A reactive oxygen species assay kit (cat# S0033S) and adenosine triphosphate (ATP) activity assay kit (cat# S0027) were purchased from Beyotime Biotechnology (Shanghai, China). Additionally, *o*-nitrophenyl-β-D-galactopyranoside (ONPG) and 3-[4,5-dimethylthiazol-2-yl]-2,5-diphenyl tetrazolium bromide (MTT) were purchased from Shanghai Aladdin Bio-Chem Technology Co., Ltd (Shanghai, China).

2.2. Synthesis of Cu_2O and Au@Cu_2O nanocubes

A hydrothermal method was employed to prepare Cu_2O, in line with a previous report.[34] Briefly, 500 mL of $CuCl_2$ solution (0.01 M) was placed in a water bath at 55 °C, and then 50 mL of NaOH solution (2 M) was added dropwise to the $CuCl_2$ solution under vigorous stirring. Stirring was performed for another 30 min. After that, 50 mL of ascorbic acid (0.6 M) was added to the mixed solution under continuous stirring for 5 h. The brick red products were collected *via* centrifugation (7000 rpm) and then washed with deionized water and ethanol five times each. Finally, the obtained products were dried in an oven at 30 °C for 6 h.

2.3. Synthesis of Au@Cu_2O nanocubes

The Au@Cu_2O hybrid nanocubes were prepared *via* the photoreduction of $HAuCl_4$ on Cu_2O.[35] Briefly, 100 mg of Cu_2O was dispersed in 15 mL of deionized water. To prepare Au@Cu_2O nanocubes with different amounts of Au, 10 ml of $HAuCl_4$ solution with different $HAuCl_4$ contents (0.0625 g L^{-1}, 0.25 g L^{-1}, and 2.5 g L^{-1}) were added to the Cu_2O suspension under vigorous stirring and irradiation with a Xe lamp (operation current = 5 A, SXE-300 W, Beijing Changming Technology Co. Ltd). After that, the mixture was further irradiated for 1 h. The obtained products were collected by centrifugation and then washed with deionized water and ethanol three times each. The final products were dried in an oven at 30 °C for 6 h. The resulting samples were named Au(0.625)@Cu_2O, Au(2.5)@Cu_2O, and Au(25)@Cu_2O according to the amount of $HAuCl_4$ used.

2.4. Characterization of Cu_2O and Au@Cu_2O nanocubes

The surface morphologies of different samples were imaged using a field emission scanning electron microscope (FE-SEM, Zeiss Sigma 500, Germany) and transmission electron microscope (TEM, TF20, FEI, USA). Elemental mapping images were taken on the above-mentioned TEM. The phase structure and chemical composition of different samples were characterized using X-ray diffraction (XRD, D8A25, Bruker, Germany) and X-ray photoelectron spectroscopy (XPS, Escalab 250Xi, USA), respectively.

2.5. Electrochemistry measurements

All electrochemistry measurements were carried out on an electrochemical analysis workstation (CHI660E, Shanghai Chenhua Instrument Co. Ltd, China), with samples on indium tin oxide glass serving as the working electrode, a saturated calomel electrode serving as the reference electrode, and a platinum plate electrode serving as the counter electrode in 0.5 M $NaSO_4$ electrolyte solution. The electrochemical impedance spectrum (EIS) was measured in the A.C. Impedance mode. To investigate the US current, US stimulation was applied using an Intelect Mobile Ultrasound (Chattanooga 2776, DJO Group, USA), and the parameters were set as follows: 1.5 W cm^{-2}, continuous, 1 MHz. The generated US current of different samples was measured in the amperometric *i–t* curve mode.

2.6. ROS generation analysis

A commercial reactive oxygen species assay kit was used to evaluate the level of ROS generated by different samples with US stimulation (1.5 W cm^{-2}, 50% duty cycle, 1 MHz, 15 min). Briefly, 10 μL of 2′,7′-dichlorodihydrofluorescein diacetate (DCFH-DA) solution (10 mM) was dispersed in 45 μL of ethanol and then mixed with 200 μL of NaOH solution (0.1 M) for 30 min under stirring at room temperature in dark conditions. Then, the solution was diluted with 1 mL of PBS. Different samples were mixed with the obtained solution and stimulated by US for 15 min as mentioned above. Finally, the fluorescence intensity of 2′,7′-dichlorofluorescein (DCF) was measured at 525 nm with excitation at 485 nm by a microplate reader (SpectraMax i3, Molecular Devices, USA).

2.7. Antibacterial evaluation

5 μL of the *Staphylococcus aureus* (*S. aureus*) suspension (≈3 × 10^9 CFU mL^{-1}) was diluted into 500 μL of 0.25 mg mL^{-1} Cu_2O or Au@Cu_2O nanocubes in centrifuge tubes. Then, US stimulation with an intensity of 1.5 W cm^{-2} in 50% duty cycle at 1 MHz for 15 min was used to treat the bacterium-sample mixed suspension in subsequent experiments according to the previous protocols.[36] After that, 20 μL of the treated bacteria suspension was collected and spread on Luria–Bertani (LB) agar and incubated at 37 °C for 24 h. The number of colonies (N) on each LB agar plate was counted, and the antibacterial ratio was calculated as follows: antibacterial ratio (%) = [N(control) − N(experiment group)]/N(control) × 100%.

2.7.1. Morphology of the attached bacteria. Bacteria were first treated with samples as described above. Then, the samples with bacteria were fixed with glutaraldehyde (2.5%), washed by PBS, and then dehydrated with gradient ethanol solution (30, 50, 70, 90, and 100% v/v) for 15 min each time. After that, the morphology of bacteria was observed under an FE-SEM.

2.7.2. ATP activity. ATP is an important energy molecule that participates in bacteria metabolism.[37] A commercial ATP activity assay kit was used to evaluate the ATP levels of bacteria treated with different samples after US stimulation. Briefly, 20 μL of the bacteria suspension (1 × 10^9 CFU mL^{-1}) was treated with different samples (500 μL, 0.25 mg mL^{-1}) under US stimulation for 15 min. After that, the solution was centrifuged at a speed of 12 000g at 4 °C for 5 min and then resuspended in 400 μL of ATP lysis buffer. Then, the lysis buffer solution was treated with an ultrasonic cell disruptor (vcx500, Sonics, USA) at the following operating settings: 30% power, 3 s on/5 s off, 5 min. Finally, the upper layer solution was collected and measured using a microplate reader according to the manufacturer's guidelines.

2.7.3. Intracellular ROS level in bacterial cells. A commercial reactive oxygen species assay kit was used to evaluate the level of intracellular ROS in bacteria treated with different samples under US stimulation. Briefly, 1 mL of bacteria suspension (7 × 10^9 CFU mL^{-1}) was first centrifuged at a speed of 6000 rpm for 5 min and then washed with PBS *via* centrifugation three times. The obtained bacteria were resuspended in 1 mL of PBS, cultured with 1 μL of DCFH-DA solution (10 mM), and incubated at 37 °C in a shaker incubator for 30 min. Then, the mixture was treated with US stimulation. Finally, 100 μL of the treated bacteria were added to a 96-well plate, and the relative fluorescence intensity of DCF was detected at 525 nm with excitation at 485 nm using a microplate reader.

2.7.4. Bacterial membrane permeability. ONPG was used to measure the impact of different samples on the permeability of the bacteria membrane under US stimulation. First, bacteria (7 × 10^9 CFU mL^{-1}) were cultured with isopropyl β-D-1-thiogalactopyranoside (IPTG) at 37 °C for 12 h. Next, bacteria were collected by centrifugation at a speed of 6000 rpm for 5 min and then washed with PBS three times. After that, the treated bacteria suspension with different samples was stimulated by US (1.5 W cm^{-2}, 50%, 1 MHz, 15 min). Finally, 15 μL of the US-treated bacteria was mixed with 15 μL of ONPG (12.5 mM), 10 μL of dimethyl sulfoxide (7%), and 110 μL of PBS in a 96-well plate. The absorbance at 420 nm was measured using a microplate reader.

2.8. Coating of RBC membranes onto Au(25)@Cu_2O (RBC-Au(25)@Cu_2O)

To obtain RBC membranes, whole rat blood was centrifuged at 3000 rpm for 5 min to remove the serum and buffy coat in the supernatant. The resulting products were then washed with ice-cold PBS *via* centrifugation before resuspending in 0.25× PBS for hemolysis at 4 °C for 24 h. After that, the hemoglobin was removed *via* centrifugation at a speed of 13 000 rpm for 10 min with 0.25× PBS. This was performed several times until the supernatant was colorless. Finally, the RBC membranes with a pink color were collected to coat onto Au(25)@Cu_2O. Au(25)@Cu_2O nanocubes were first ultrasonically mixed with RBC membranes in PBS. Then, the mixture was extruded 10 times through a 1 μm polycarbonate porous membrane with a mini extruder (Avanti, USA). Finally, the obtained RBC-Au(25)@Cu_2O was collected and stored at 4 °C for further use.

2.9. Evaluation of cytocompatibility

Cytocompatibility was evaluated with 3-[4,5-dimethylthiazol-2-yl]-2,5-diphenyl tetrazolium bromide (MTT) assays. Different

samples and a control group were cultured with mouse embryonic fibroblast cells (NIH3T3) in 96-well plates for 1 day. The culture medium was refreshed every other day. At each time point, 200 μL of MTT solution (5 mg mL^{-1} in PBS) was added to each well after removal of the culture medium, and then the cells were incubated at 37 °C for another 4 h. After that, 100 μL of dimethyl sulfoxide (DMSO) was added to each well, followed by shaking on a shaking table for 15 min to dissolve formazan crystals. Finally, the absorbance was measured at 570 nm by a microplate reader (SpectraMax i3, Molecular Devices). The percentage of cell viability was calculated by dividing the absorbance readings of samples by that of the control group.

2.10. Statistical analysis

All the quantitative data were evaluated as mean values ± SD of repeated experiments (n = 3). A one-way analysis of variance (ANOVA) program combined with a Student t-test was used to evaluate the statistical significance of the variance. Values of $^{*}P < 0.05$ and $^{**}P < 0.01$ were considered statistically significant.

3. Results and discussion

3.1. Synthesis and characterization of Au@Cu_2O hybrid nanocubes

As illustrated in Fig. 1a, the first step of synthesizing Au@Cu_2O nanocubes was to prepare Cu_2O nanocubes. After that, Au@Cu_2O hybrid nanocubes with different loading amounts of Au were synthesized by adding different amounts of $HAuCl_4$ under irradiation with a Xe lamp. The final products, which were prepared with 0.625 mg, 2.5 mg, and 25 mg of $HAuCl_4$, were named Au(0.625)@Cu_2O, Au(2.5)@Cu_2O, and Au(25)@Cu_2O, respectively.

Fig. 1b shows the regular cubic shapes of Cu_2O and Au@Cu_2O hybrid nanocubes. The magnified images shown in Fig. 1c reveal that the surface of the Cu_2O nanocubes was smooth and flat. Small Au nanoparticles could be observed on all Au@Cu_2O hybrid nanocubes, and their morphologies varied with the loading amount of Au. On Au(0.625)@Cu_2O, Au nanoparticles were sparsely deposited on Cu_2O nanocubes without completely covering the surface of the cubic Cu_2O. With greater loading amounts of Au, the Au nanoparticles were distributed evenly on the surface of Cu_2O on Au(2.5)@Cu_2O, with an increased coverage ratio. If the loading amount of Au was further increased, the deposited Au nanoparticles became much denser and randomly packed on Au(25)@Cu_2O. The Cu_2O nanocubes were fully covered by Au nanoparticles. The morphology of the cubic structure and deposition of different amounts of Au nanoparticles on different samples were confirmed by TEM (Fig. 1d). Fig. 1e shows the elemental mapping images of Au and Cu, which reveal the increasing amount of Au on the Au(0.625)@Cu_2O, Au(2.5)@Cu_2O, and Au(25)@Cu_2O samples and the uniform distribution of Au on the Cu_2O nanocubes.

The phase structure of Cu_2O and Au@Cu_2O nanocubes was characterized by XRD. As shown in Fig. 2a and reported in previous studies,[28] the diffraction peaks of Cu_2O nanocubes matched with the cubic Cu_2O crystal. After deposition of Au nanoparticles, a new diffraction peak located at 38.18° could be detected, which was indexed to the (111) crystal plane of face-centered cubic Au.[38] The relative intensity of this diffraction peak indicates varied contents of Au in different Au@Cu_2O samples. The highest intensity was found on Au(25)@Cu_2O.

The chemical composition of different samples was studied by XPS, and all peaks were calibrated to the binding energy of C 1s at 284.8 eV. The survey spectra of XPS patterns, which are shown in Fig. 2b, indicate the presence of Cu 2p and Au 4f. This confirms the successful deposition of Au on Cu_2O nanocubes. The fine-scan XPS spectra of Cu and Au are shown in Fig. 2c and d, respectively. Fig. 2c shows the fine scan XPS spectra of Cu 2p. The two peaks with binding energies of 932.1 eV (Cu $2p^{3/2}$) and 952.1 eV (Cu $2p^{1/2}$) could be assigned to the lattice Cu^{+} originating from Cu_2O.[39,40] The shakeup satellite peaks were the features of $3d^9$ shells of Cu in the ground state (Cu^{2+}), indicating the presence of CuO.[41] To be specific, the peaks Cu $2p^{3/2}$ and Cu $2p^{1/2}$ of Au(25)@Cu_2O shifted to 933.8 eV and 953.7 eV, respectively. This result indicated that the Cu_2O at the surface of Au(25)@Cu_2O had been completed oxidized.[42,43] Fig. 2d shows the two peaks of Au 4f with binding energies of 84.0 (Au $4f^{7/2}$) and 87.5 eV (Au $4f^{5/2}$), which can be assigned to Au(0).[44] The intensity of these two peaks increased with greater loading amounts of Au. A slight red shift could be observed on Au 4f peaks when the loading amount of Au was increased.

3.2. Investigation of sonodynamic effects

The peak shifts shown in the XPS results indicate a strong electron interaction and charge transfer between Cu_2O and Au, which can be attributed to the formation of a Schottky contact.[38] The work function of the p-type semiconductor (W_s) Cu_2O is 5.27 eV, and that of the metal (W_m) Au is 5.10 eV.[45] This satisfies the $W_s > W_m$ criteria for forming a Schottky junction at the interface of the p-type semiconductor and metal. Once Au was deposited onto the surface of Cu_2O cubes, electrons were transferred from Au to Cu_2O at the interface. The Fermi level of Cu_2O (E_{fs}) had increased until it reached the equilibrium state (E_f) with the Fermi level of Au (E_{fm}) (illustrated in Fig. 3a).

Fig. 3b shows the EIS curves of different samples and the corresponding equivalent circuit and fitting results are shown in Fig. S1 and Table S1.† The trend of electric impendence was in the following order: Au(25)@Cu_2O < Au(2.5)@Cu_2O < Au(0.625)@Cu_2O < Cu_2O. Thus, the electron transfer resistance had been reduced with greater loading amounts of Au, indicating that Au loaded on Cu_2O nanocubes could favor charge transfer.[46] Similar to light illumination, US can induce electron motion in metals and semiconductors because of the acoustoelectric effect.[47] As illustrated in Fig. 3a, when stimulated by US, the electrons of Cu_2O were excited from their

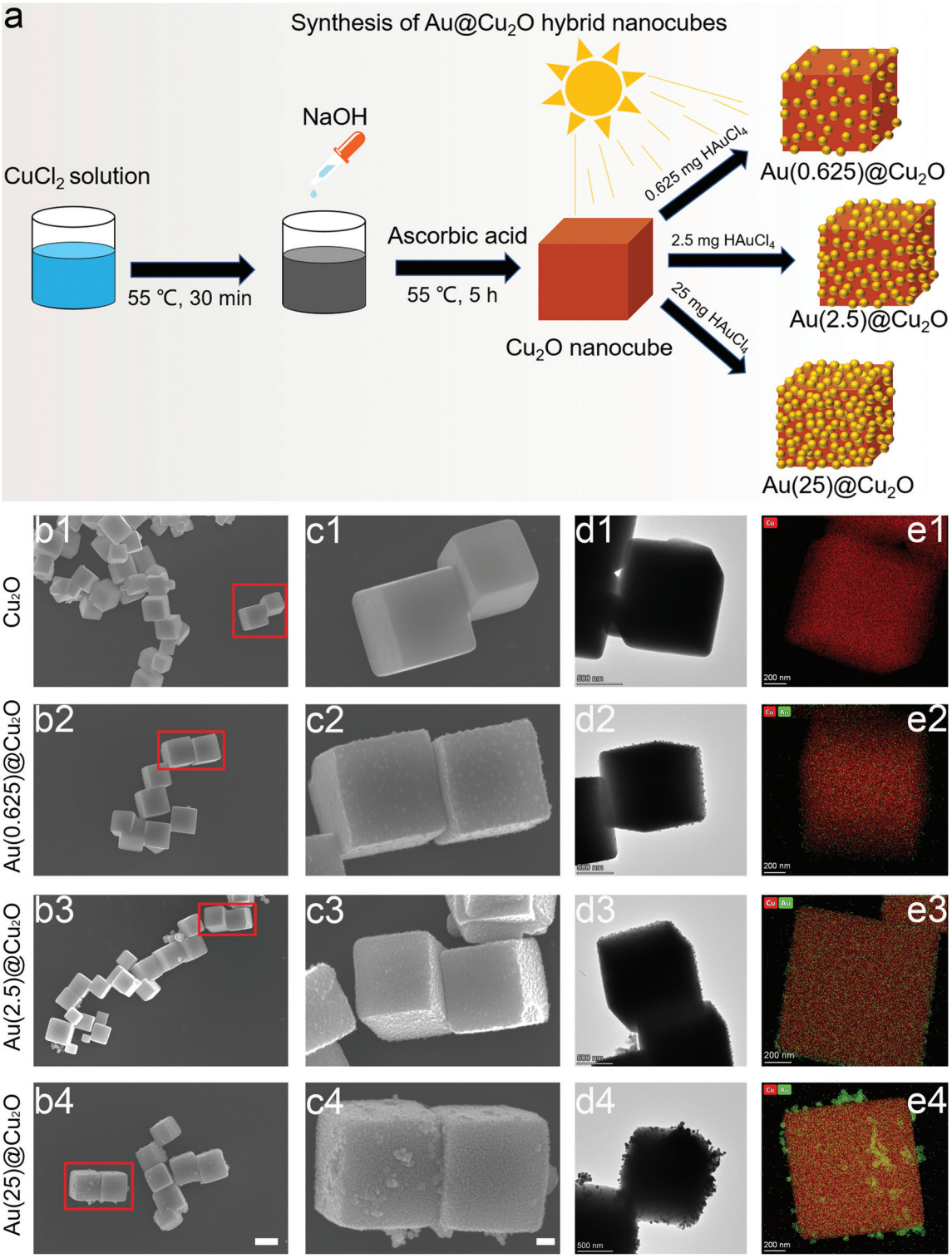

Fig. 1 Synthesis and characterization of Au@Cu_2O hybrid nanocubes. (a) Schematic illustration of the synthesis process. (b) and (c) Representative FE-SEM images of Cu_2O, Au(0.625)@Cu_2O, Au(2.5)@Cu_2O, and Au(25)@Cu_2O; scale bars:1 μm and 200 nm, respectively. (d) TEM images of Cu_2O, Au (0.625)@Cu_2O, Au(2.5)@Cu_2O, and Au(25)@Cu_2O; scale bar:500 nm. (e) Elemental mapping images of Cu_2O, Au(0.625)@Cu_2O, and Au(2.5)@Cu_2O; scale bar:200 nm.

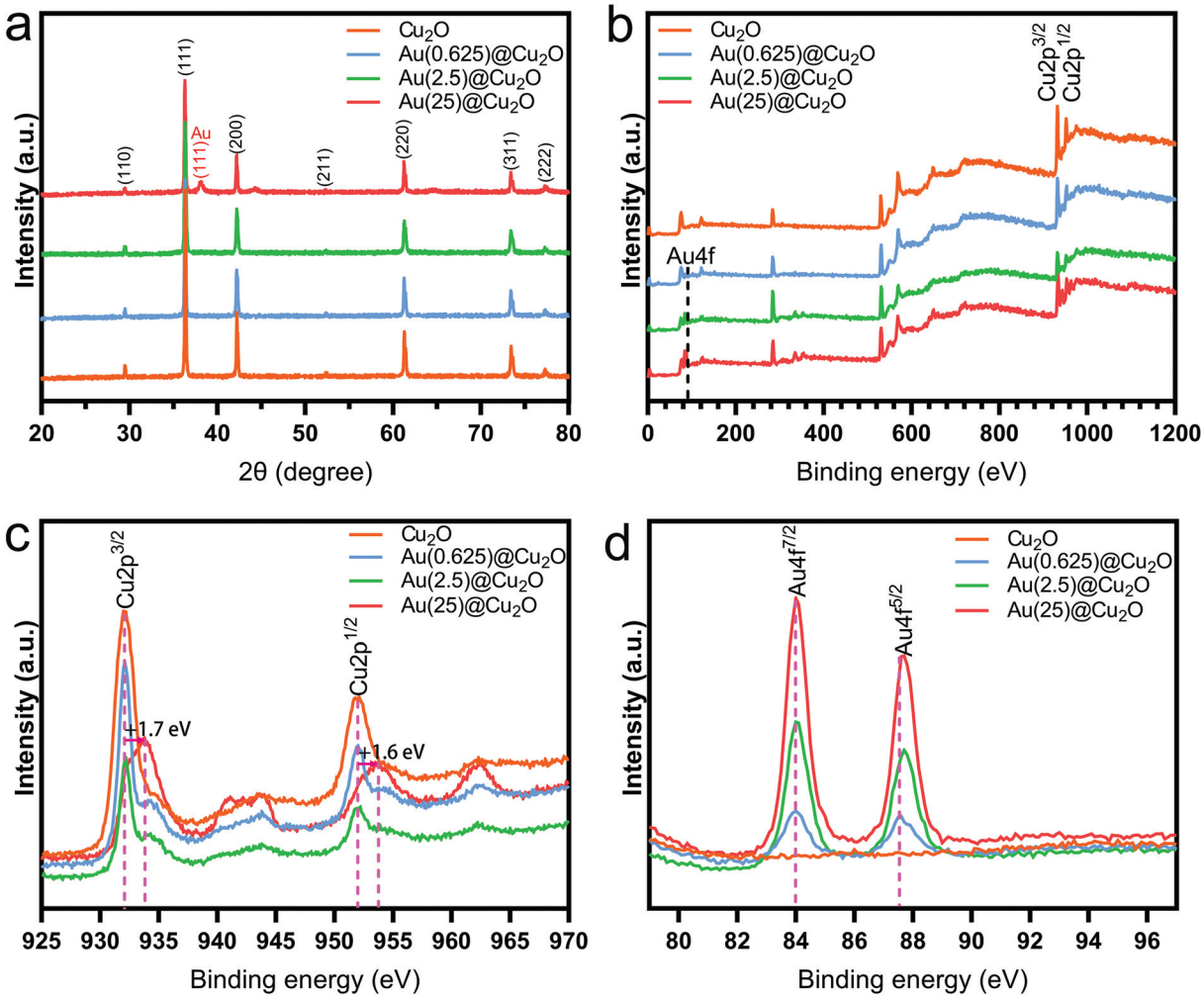

Fig. 2 The phase structure and chemical composition of Cu_2O and Au@Cu_2O nanocubes. (a) XRD patterns. (b) XPS spectra, with the survey scan ranging from 0 to 1200 eV. (c) XPS spectrum survey of the Cu 2p band. (d) XPS spectrum survey of the Au 4f band.

valence band (VB) to conduction band (CB), where the edge is higher than the Fermi level of Au. Thus, these US-excited electrons on the CB of Cu_2O could transfer to Au. In addition, the Schottky barrier could block the backflow of electrons, facilitating electron–hole separation. Thus, we next measured the US current generation of different samples under US stimulation (1.5 W cm^{-2}, continuous, 1 MHz). Fig. 3c shows that the intensities of the US current can be ordered as follows: Au(25)@Cu_2O > Au(2.5)@Cu_2O > Au(0.625)@Cu_2O > Cu_2O. This was consistent with the EIS results, indicating greater production of US-excited electrons and a higher charge transfer efficiency on samples with a greater loading amount of Au. Given the difference between Au(0.625)@Cu_2O and Au(2.5)@Cu_2O, Au(25)@Cu_2O was the surface coverage of Au on Cu_2O (morphologies are shown in Fig. 1). We presume that the increased surface coverage of Au would favor a Schottky contact between Au and Cu_2O and facilitate unidirectional electron transfer, thereby improving the electron–hole separation efficiency. These results indicate that the US-electric properties of the Au@Cu_2O nanocubes could be tuned by changing the loading amount of Au. Next, the ROS generation ability of different samples was investigated. DCFH-DA is nonfluorescent, but it can be oxidized to DCF with fluorescence by ROS.[48] As shown in Fig. 3d, Cu_2O could produce a small amount of ROS after stimulation by US for 15 min. In comparison, all Au@Cu_2O samples produced more ROS, indicating that Au doping could significantly increase ROS generation. Among the three Au@Cu_2O nanocubes, ROS generation ability could be sorted as follows: Au(25)@Cu_2O > Au(2.5)@Cu_2O > Au(0.625)@Cu_2O. This agrees with the above results, indicating that higher electron–hole separation efficiency could favor ROS generation.

3.3. Evaluation of antibacterial activity

To investigate the antibacterial activity of different samples under US stimulation, samples were mixed with the bacteria suspension in centrifuge tubes and placed on a US probe (illustrated in Fig. 4a). *S. aureus*, an invasive Gram-positive bacterium that is responsible for a wide range of diseases and could be fatal,[49,50] was selected to evaluate the antibacterial ability of different samples with or without US stimulation. As

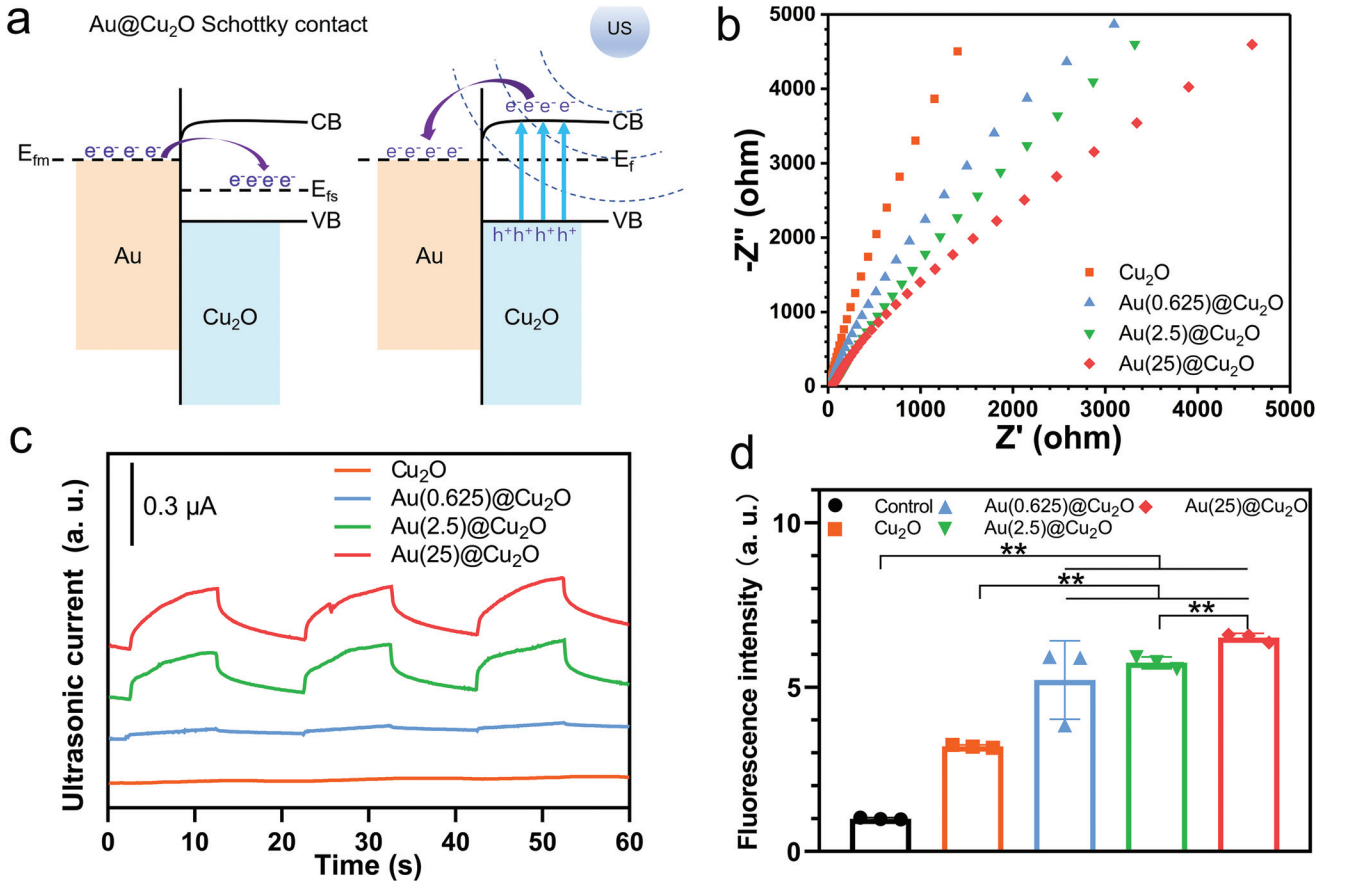

Fig. 3 Evaluation of sonocatalytic activity and ROS generation ability. (a) Schematic diagram of a Schottky contact between Au and Cu_2O. (b) Electrochemical impedance spectra of different samples. (c) US current curves of different samples under US stimulation. (d) ROS generation abilities of different samples detected by the fluorescence intensity of DCF. n = 3 independent experiments per group; *P < 0.05 and **P < 0.01.

shown in Fig. 4b, viable colonies of bacteria with all samples grew quite well on LB agar plates without US stimulation. After stimulation by US for 15 min, no significant decrease in the survival of colonies was observed for the control group and Cu_2O nanocubes. However, after loading Au on Cu_2O, all Au@Cu_2O hybrid nanocubes exhibited significantly increased antibacterial abilities. Specifically, the antibacterial ratio of Au(0.625)@Cu_2O was 91.37%. When the loading amount of Au was further increased, the antibacterial ratios of Au(2.5)@Cu_2O and Au(25)@Cu_2O reached 99.15% and 99.67%, respectively. This trend in the antibacterial ability of different samples aligned with the US current intensity and ROS generation ability, indicating that the antibacterial ability of the Au@Cu_2O hybrid nanocubes could be adjusted by tuning the Schottky contact area between Cu_2O and Au.

ATP is the major intracellular energy source of bacteria, and it is essential in the metastasis process.[51,52] Decreased ATP levels could indicate the inactivation or death of bacteria. Fig. 4d shows the ATP levels in bacteria treated with different samples under US stimulation for 15 min. The luminescence intensity of ATP in Cu_2O-treated bacteria was lower than the control group and decreased dramatically in Au@Cu_2O hybrid nanocube-treated bacteria. This indicates that the rapid bacteria-killing ability was subject to a higher ratio of Au deposition on Cu_2O under US stimulation.

3.4. Antibacterial underlying mechanism

Cu_2O and Au(25)@Cu_2O were selected as the representative groups to further investigate the antibacterial mechanism. First, SEM was utilized to observe the morphology of bacteria treated with different samples with or without US stimulation. As shown in Fig. 5a, *S. aureus* exhibited the typical spherical shapes with a smooth surface and boundaries in the control group without US stimulation. In line with the antibacterial results shown in Fig. 4b, the morphology of bacteria remained intact after treatment with US in the Cu_2O and control groups. However, when the bacteria were mixed with Au(25)@Cu_2O and stimulated by US for 15 min, the membranes of *S. aureus* were damaged and the spherical shape became wrinkled (highlighted by red arrows in Fig. 5a), indicating the death of bacteria.[5,53] As a nonfluorescent probe, DCFH-DA can be easily loaded into bacteria. Then, the esterase within bacteria can hydrolyze DCFH-DA to DCFH, which reacts with ROS to form DCF.[54] The ROS levels within bacteria after treatment with samples under 15 min US stimulation were detected by measuring the intracellular fluorescence intensity of DCF. As

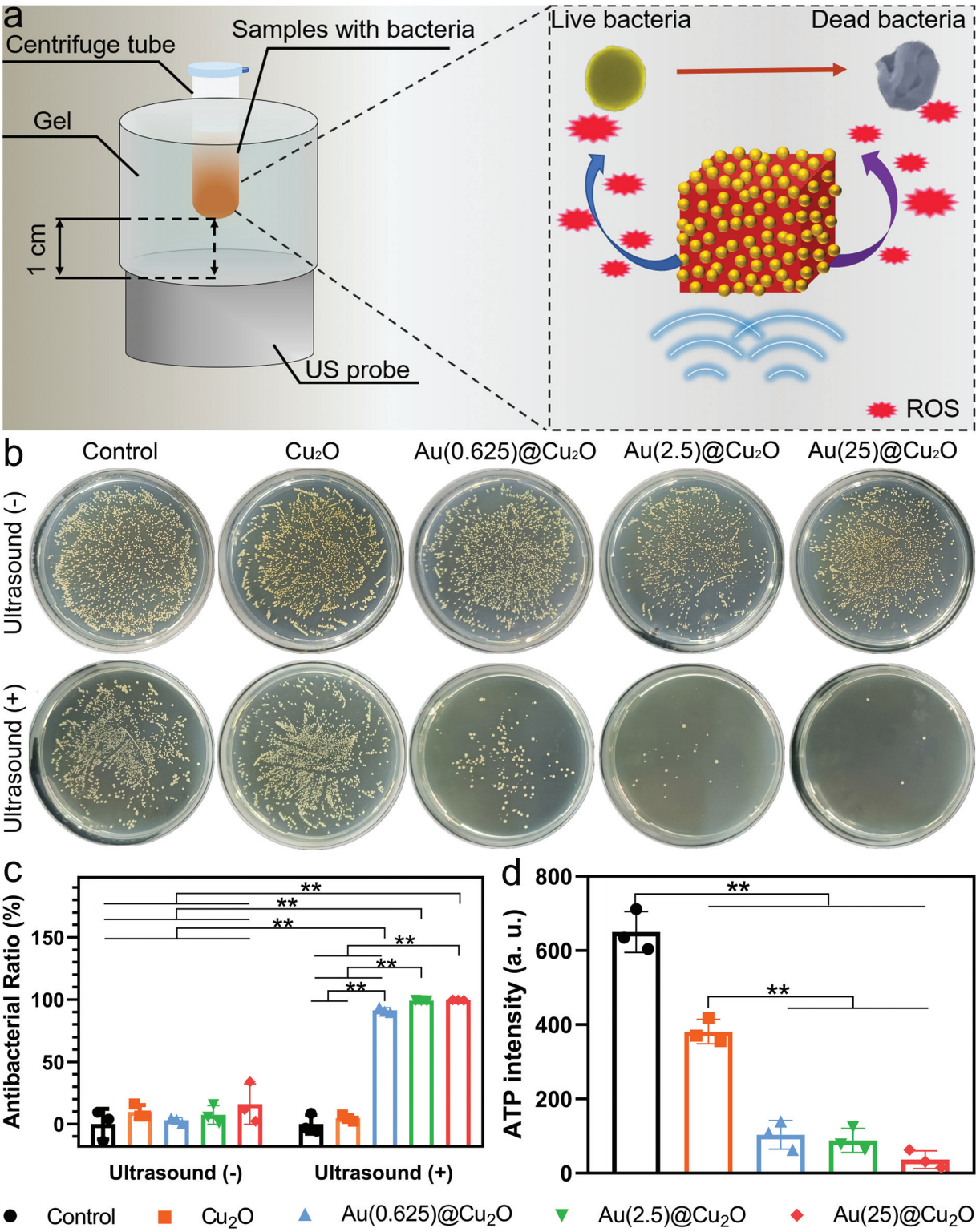

Fig. 4 Evaluation of the antibacterial activity of different samples against *S. aureus*. (a) Schematic illustration of antibacterial ability against *S. aureus* under US stimulation. (b) Spread plates of different samples with or without US stimulation. (c) The corresponding antibacterial ratio. (d) ATP levels of bacteria treated with different samples under US stimulation. n = 3 independent experiments per group; $^{*}P < 0.05$ and $^{**}P < 0.01$.

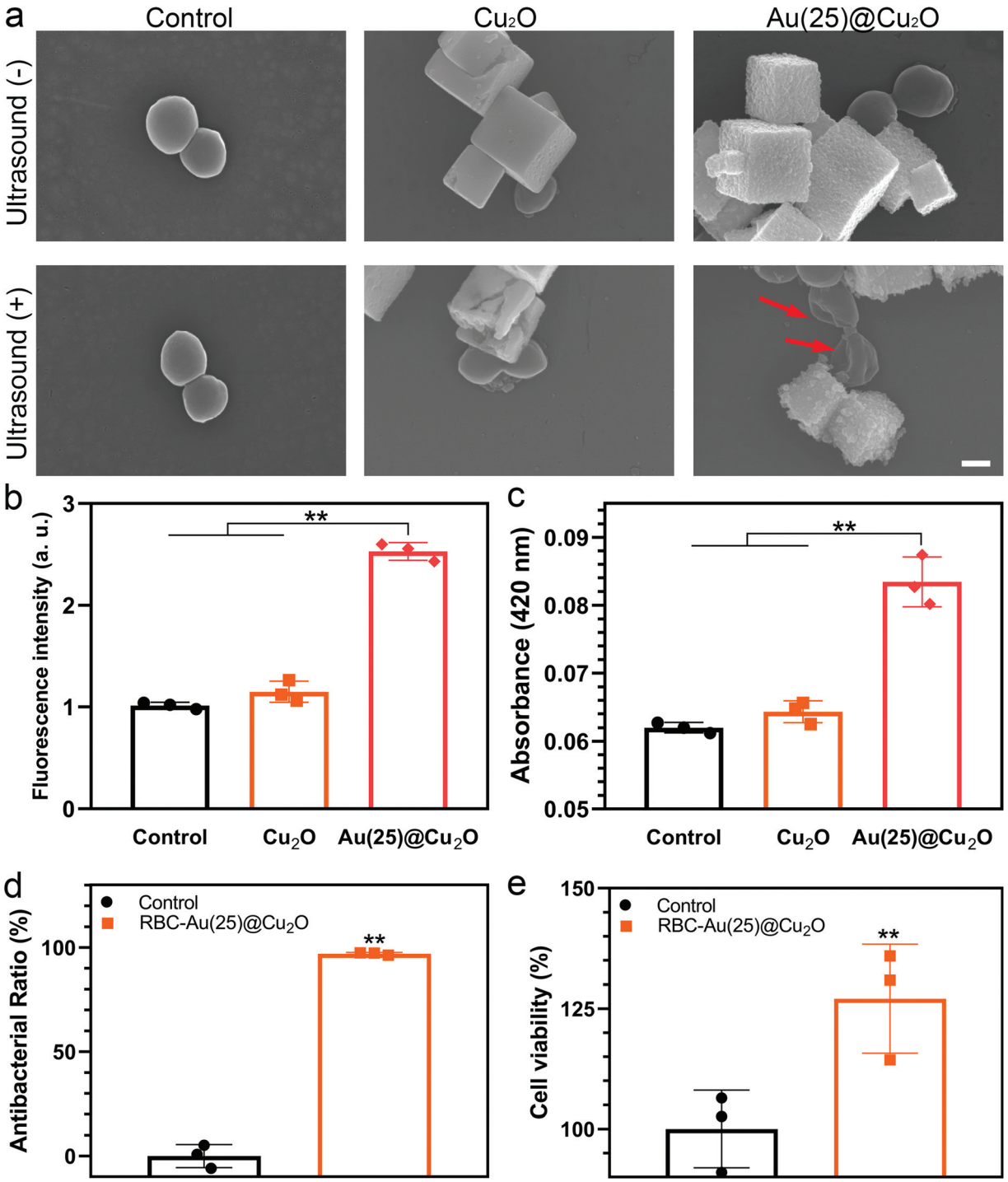

Fig. 5 Antibacterial mechanism study and evaluation of biocompatibility. (a) Morphologies of bacteria treated with Cu_2O and Au(25)@Cu_2O with or without US stimulation; scale bar: 500 nm. (b) Intracellular ROS detected by the fluorescence intensity of DCF. (c) Membrane permeability of the bacteria investigated by ONPG. (d) Antibacterial ratio of RBC-Au(25)@Cu_2O against *S. aureus* under US stimulation. (e) Cell viability was measured by MTT assay after culturing with RBC-Au(25)@Cu_2O for 1 day. n = 3 independent experiments per group; *P < 0.05 and **P < 0.01.

shown in Fig. 5b, significantly stronger fluorescence was found in the Au(25)@Cu_2O-treated bacteria after stimulation by US for 15 min. This indicates a higher intracellular ROS level in the Au(25)@Cu_2O-treated bacteria. The elevated ROS level significantly enhanced the oxidative stress within bacteria, which could influence the metabolism of bacteria—or even kill them—by reacting with intracellular compounds.[12–14] ONPG hydrolysis detection was used to measure the cell membrane permeability.[55,56] As shown in Fig. 5c, the significantly higher absorbance at OD 420 indicated that Au(25)@Cu_2O increased

the membrane permeation of bacteria, which is consistent with the distorted bacterial morphology observed under an FE-SEM (Fig. 5a). These results suggested that Au(25)@Cu_2O could rapidly kill *S. aureus* under US stimulation due to the elevated oxidative stress and bacterial membrane disruption.

3.5. Evaluation of biocompatibility

Next, to evaluate the biocompatibility of different samples, NIH3T3 cells were selected to conduct MTT assays. As shown in Fig. S2,† bare Cu_2O and Au@Cu_2O exhibited inferior cytotoxicity. The RBC membrane as a natural circulating carrier and stabilizer has been adopted to reduce the cytotoxicity of nanomaterials for some time.[57,58] In fact, previous studies had demonstrated the cytocompatibility and long-term applicability of nanoparticles coated with RBC membranes.[36,59] Thus, to improve the biocompatibility of Au@Cu_2O hybrid nanocubes, we modified Au(25)@Cu_2O with a coating of RBC membrane. The cell viability of RBC-Au(25)@Cu_2O was measured by MTT (Fig. 5e). We found that the cell viability of RBC-Au(25)@Cu_2O increased to 127.04% compared with the control group due to the superior biocompatibility of RBC membranes. This indicates that the cytotoxicity of RBC-Au(25)@Cu_2O was resolved. It has been proven that cell membranes refine the biocompatibility of nanomaterials,[60,61] as the membrane proteins serve as camouflage, concealing nanomaterials from natural tissue responses. Then, the antibacterial ability of RBC-Au(25)@Cu_2O after RBC membrane coating was evaluated (Fig. 5d and Fig. S3†). Although the antibacterial ratio of RBC-Au(25)@Cu_2O against *S. aureus* slightly decreased compared with bare Au(25)@Cu_2O, the antibacterial ratio still reached 96.96%.

4. Conclusions

We proposed a series of effective sonosensitizers for rapid bacterial elimination that rely on the construction of a Schottky junction between Au nanoparticles and Cu_2O nanocubes. Au@Cu_2O hybrid nanocubes with higher loading amounts of Au exhibited better sonocatalytic properties. A Schottky contact between Au and Cu_2O facilitated superior electron–hole separation, which significantly improved ROS generation and antibacterial efficiency against *S. aureus* under US stimulation. With a coating of an RBC membrane, the cytotoxicity of Au@Cu_2O hybrid nanocubes was substantially reduced without compromising their original antibacterial properties. We believe that this concept (*i.e.*, construction of a Schottky contact between the metal and semiconductor counterparts to eliminate bacteria) can be extended to other types of metals and semiconductors. We hope our work paves a way for the development of better sonosensitizers for a variety of bacterial treatments.

Author contributions

Y. Z., X. L., S. W., and K. W. K. Y. conceived and designed the concept of the experiments. Y. Z. and W. H. synthesized the materials and conducted the characterization and assays. Y. Z., W. H., S. W. and K. W. K. Y. analyzed the experimental data and cowrote the manuscript. L. T., J. W., C. M., Y. X. and K. M. C. C. provided important experimental insights.

Conflicts of interest

There are no conflicts to declare.

Acknowledgements

This work was jointly supported by the National Key R&D Program of China (2018YFA0703100), Hong Kong Research Grant Council (no. 17207719 and 17214516), Hong Kong Health and Medical Research Fund no. 19180712, the China National Funds for Distinguished Young Scientists (no. 51925104), HKU-SZH Fund for Shenzhen Key Medical Discipline (SZXK2020084), Shenzhen Science and Technology Funding (JSGG20180507183242702) and Sanming Project of Medicine in Shenzhen "Team of Excellence in Spinal Deformities and Spinal Degeneration" (SZSM201612055).

References

1 S. Nolivos, J. Cayron, A. Dedieu, A. Page, F. Delolme and C. Lesterlin, *Science*, 2019, **364**, 778–782.
2 A. Zipperer, M. C. Konnerth, C. Laux, A. Berscheid, D. Janek, C. Weidenmaier, M. Burian, N. A. Schilling, C. Slavetinsky, M. Marschal, M. Willmann, H. Kalbacher, B. Schittek, H. Brotz-Oesterhelt, S. Grond, A. Peschel and B. Krismer, *Nature*, 2016, **535**, 511–516.
3 S. Agnihotri, S. Mukherji and S. Mukherji, *Nanoscale*, 2013, **5**, 7328–7340.
4 A. K. Suresh, D. A. Pelletier and M. J. Doktycz, *Nanoscale*, 2013, **5**, 463–474.
5 J. Li, L. Tan, X. Liu, Z. Cui, X. Yang, K. W. K. Yeung, P. K. Chu and S. Wu, *ACS Nano*, 2017, **11**, 11250–11263.
6 Y. Zhu, X. Liu, K. W. K. Yeung, P. K. Chu and S. Wu, *Appl. Surf. Sci.*, 2017, **400**, 14–23.
7 S. Saidin, M. A. Jumat, N. A. A. Mohd Amin and A. S. Saleh Al-Hammadi, *Mater. Sci. Eng., C*, 2021, **118**, 111382.
8 Y. Li, X. Liu, L. Tan, Z. Cui, X. Yang, Y. Zheng, K. W. K. Yeung, P. K. Chu and S. Wu, *Adv. Funct. Mater.*, 2018, **28**, 1800299.
9 X. Kong, X. Liu, Y. Zheng, P. K. Chu, Y. Zhang and S. Wu, *Mater. Sci. Eng., R*, 2021, **145**, 100610.
10 B. Tian, C. Wang, S. Zhang, L. Feng and Z. Liu, *ACS Nano*, 2011, **5**, 7000–7009.
11 C. A. Robertson, D. H. Evans and H. Abrahamse, *J. Photochem. Photobiol., B*, 2009, **96**, 1–8.
12 S. Liu, T. H. Zeng, M. Hofmann, E. Burcombe, J. Wei, R. Jiang, J. Kong and Y. Chen, *ACS Nano*, 2011, **5**, 6971–6980.

13 M. P. Brynildsen, J. A. Winkler, C. S. Spina, I. C. MacDonald and J. J. Collins, *Nat. Biotechnol.*, 2013, **31**, 160–165.
14 J. A. Imlay, *Nat. Rev. Microbiol.*, 2013, **11**, 443–454.
15 C. Wang, J. Li, X. Liu, Z. Cui and S. Wu, *Biomater. Sci.*, 2020, **8**, 4216–4224.
16 W. Fan, P. Huang and X. Chen, *Chem. Soc. Rev.*, 2016, **45**, 6488–6519.
17 X. Pang, X. Liu, Y. Cheng, C. Zhang, E. Ren, C. Liu, Y. Zhang, J. Zhu, X. Chen and G. Liu, *Adv. Mater.*, 2019, **31**, 1902530.
18 X. Wang, X. Zhong, F. Gong, Y. Chao and L. Cheng, *Mater. Horiz.*, 2020, **7**, 2028–2046.
19 J. E. Kennedy, *Cancer*, 2005, **5**, 321–327.
20 M. Wu, Z. Zhang, Z. Liu, J. Zhang, Y. Zhang, Y. Ding, T. Huang, D. Xiang, Z. Wang, Y. Dai, X. Wan, S. Wang, H. Qian, Q. Sun and L. Li, *Nano Today*, 2021, **37**, 101104.
21 M. Song, Y. Cheng, Y. Tian, C. Chu, C. Zhang, Z. Lu, X. Chen, X. Pang and G. Liu, *Adv. Funct. Mater.*, 2020, **30**, 2003587.
22 S. Bai, N. Yang, X. Wang, F. Gong, Z. Dong, Y. Gong, Z. Liu and L. Cheng, *ACS Nano*, 2020, **14**, 15119–15130.
23 M. Han, S. Zhu, S. Lu, Y. Song, T. Feng, S. Tao, J. Liu and B. Yang, *Nano Today*, 2018, **19**, 201–218.
24 S. Liang, X. Deng, G. Xu, X. Xiao, M. Wang, X. Guo, P. A. Ma, Z. Cheng, D. Zhang and J. Lin, *Adv. Funct. Mater.*, 2020, **30**, 1908598.
25 Y. Cao, T. Wu, W. Dai, H. Dong and X. Zhang, *Chem. Mater.*, 2019, **31**, 9105–9114.
26 M. Hara, T. Kondo, M. Komoda, S. Ikeda, J. N. Kondo, K. Domen, M. Hara, K. Shinohara and A. Tanaka, *Chem. Commun.*, 1998, **3**, 357–358.
27 L.-F. Yang, D.-Q. Chu, L.-M. Wang, G. Ge and H.-L. Sun, *RSC Adv.*, 2016, **6**, 960–966.
28 W. Zhang, B. Wang, C. Hao, Y. Liang, H. Shi, L. Ao and W. Wang, *J. Alloys Compd.*, 2016, **684**, 445–452.
29 Y.-H. Chiu, S. A. Lindley, C.-W. Tsao, M.-Y. Kuo, J. K. Cooper, Y.-J. Hsu and J. Z. Zhang, *J. Phys. Chem. C*, 2020, **124**, 11333–11339.
30 M.-Y. Kuo, C.-F. Hsiao, Y.-H. Chiu, T.-H. Lai, M.-J. Fang, J.-Y. Wu, J.-W. Chen, C.-L. Wu, K.-H. Wei, H.-C. Lin and Y.-J. Hsu, *Appl. Catal., B*, 2019, **242**, 499–506.
31 J.-M. Li, C.-W. Tsao, M.-J. Fang, C.-C. Chen, C.-W. Liu and Y.-J. Hsu, *ACS Appl. Nano Mater.*, 2018, **1**, 6843–6853.
32 Y.-K. Lin, Y.-J. Chiang and Y.-J. Hsu, *Sens. Actuators, B*, 2014, **204**, 190–196.
33 Y.-C. Pu, W.-H. Lin and Y.-J. Hsu, *Appl. Catal., B*, 2015, **163**, 343–351.
34 Y. Qin, R. Che, C. Liang, J. Zhang and Z. Wen, *J. Mater. Chem.*, 2011, **21**, 3960–3965.
35 D. Jiang, W. Zhou, X. Zhong, Y. Zhang and X. Li, *ACS Appl. Mater. Interfaces*, 2014, **6**, 10958–10962.
36 Y. Yu, L. Tan, Z. Li, X. Liu, Y. Zheng, X. Feng, Y. Liang, Z. Cui, S. Zhu and S. Wu, *ACS Nano*, 2021, **15**, 10628–10639.
37 R. Zhao, M. Lv, Y. Li, M. Sun, W. Kong, L. Wang, S. Song, C. Fan, L. Jia, S. Qiu, Y. Sun, H. Song and R. Hao, *ACS Appl. Mater. Interfaces*, 2017, **9**, 15328–15341.
38 A. Jiao, L. Xu, Y. Tian, Q. Cui, X. Liu and M. Chen, *Talanta*, 2021, **225**, 121990.
39 R. Ji, W. Sun and Y. Chu, *RSC Adv.*, 2014, **4**, 6055–6059.
40 X. Yu, J. Zhang, J. Zhang, J. Niu, J. Zhao, Y. Wei and B. Yao, *Chem. Eng. J.*, 2019, **374**, 316–327.
41 C.-K. Wu, M. Yin, S. O'Brien and J. T. Koberstein, *Chem. Mater.*, 2006, **18**, 6054–6058.
42 Q. Hua, F. Shi, K. Chen, S. Chang, Y. Ma, Z. Jiang, G. Pan and W. Huang, *Nano Res.*, 2011, **4**, 948–962.
43 Y. He, Z. S. Fishman, K. R. Yang, B. Ortiz, C. Liu, J. Goldsamt, V. S. Batista and L. D. Pfefferle, *J. Am. Chem. Soc.*, 2018, **140**, 1824–1833.
44 W. Cheng, S. Dong and E. Wang, *Langmuir*, 2003, **19**, 9434–9439.
45 B. Wang, R. Li, Z. Zhang, W. Zhang, X. Yan, X. Wu, G. Cheng and R. Zheng, *J. Mater. Chem. A*, 2017, **5**, 14415–14421.
46 J. Li, J. Wang, G. Zhang, Y. Li and K. Wang, *Appl. Catal., B*, 2018, **234**, 167–177.
47 W. Guan, L. Tan, X. Liu, Z. Cui, Y. Zheng, K. W. K. Yeung, D. Zheng, Y. Liang, Z. Li, S. Zhu, X. Wang and S. Wu, *Adv. Mater.*, 2021, **33**, 2006047.
48 W. Chen, J. Ouyang, H. Liu, M. Chen, K. Zeng, J. Sheng, Z. Liu, Y. Han, L. Wang, J. Li, L. Deng, Y. N. Liu and S. Guo, *Adv. Mater.*, 2017, **29**, 1603864.
49 L. S. Miller, V. G. Fowler, S. K. Shukla, W. E. Rose and R. A. Proctor, *FEMS Microbiol. Rev.*, 2020, **44**, 123–153.
50 Y. Yang, T. Wu, L. P. Xu and X. Zhang, *Talanta*, 2021, **226**, 122132.
51 Y. Cui, Y. Zhao, Y. Tian, W. Zhang, X. Lu and X. Jiang, *Biomaterials*, 2021, **33**, 2327–2333.
52 Y. Li, X. Liu, L. Tan, Z. Cui, D. Jing, X. Yang, Y. Liang, Z. Li, S. Zhu, Y. Zheng, K. W. K. Yeung, D. Zheng, X. Wang and S. Wu, *Adv. Funct. Mater.*, 2019, **29**, 1900946.
53 C. Mao, Y. Xiang, X. Liu, Z. Cui, X. Yang, K. W. K. Yeung, H. Pan, X. Wang, P. K. Chu and S. Wu, *ACS Nano*, 2017, **11**, 9010–9021.
54 C. Mao, Y. Xiang, X. Liu, Y. Zheng, K. W. K. Yeung, Z. Cui, X. Yang, Z. Li, Y. Liang, S. Zhu and S. Wu, *ACS Appl. Mater. Interfaces*, 2019, **11**, 17902–17914.
55 W. Hong, Y. Zhao, Y. Guo, C. Huang, P. Qiu, J. Zhu, C. Chu, H. Shi and M. Liu, *ACS Appl. Mater. Interfaces*, 2018, **10**, 10688–10705.
56 X. Zhu, Z. Ma, J. Wang, S. Chou and A. Shan, *PLoS One*, 2014, **9**, e114605.
57 W. L. Liu, M. Z. Zou, S. Y. Qin, Y. J. Cheng, Y. H. Ma, Y. X. Sun and X. Z. Zhang, *Adv. Funct. Mater.*, 2020, **30**, 2003559.
58 R. H. Fang, A. V. Kroll, W. Gao and L. Zhang, *Adv. Mater.*, 2018, **30**, 1706759.
59 L. Rao, L. L. Bu, J. H. Xu, B. Cai, G. T. Yu, X. Yu, Z. He, Q. Huang, A. Li, S. S. Guo, W. F. Zhang, W. Liu, Z. J. Sun,

H. Wang, T. H. Wang and X. Z. Zhao, *Small*, 2015, **11**, 6225–6236.
60 Q. Jiang, Z. Luo, Y. Men, P. Yang, H. Peng, R. Guo, Y. Tian, Z. Pang and W. Yang, *Biomaterials*, 2017, **143**, 29–45.
61 Z. Chai, D. Ran, L. Lu, C. Zhan, H. Ruan, X. Hu, C. Xie, K. Jiang, J. Li, J. Zhou, J. Wang, Y. Zhang, R. H. Fang, L. Zhang and W. Lu, *ACS Nano*, 2019, **13**, 5591–5601.